This is a non-peer-reviewed pre-print submitted to EarthArxiv

Role of Lithospheric and Upper-Mantle Heterogeneities in Controlling Intraplate Seismicity in Central and Southeastern Brazil

Sumit Singh[1,2*], Dip Ghosh[1#]

[1] Department of Geology, University of Calcutta, Kolkata, West Bengal 700019, India

[2] Department of Earth Sciences, Indian Institute of Technology Gandhinagar, Palaj, Gujarat 382355, India

*Corresponding author: Sumit Singh, singh.sumit@iitgn.ac.in

#dggeol_if@caluniv.ac.in

Abstract

Seismicity in Central and Southeastern Brazil is spatially heterogeneous, with active zones showing little correspondence to major geological provinces, a pattern typical of many intraplate settings worldwide. While previous studies have explored possible controls using geophysical observations, the relative roles of crustal and upper-mantle heterogeneities in shaping the regional stress fields remain poorly constrained using large-scale calculations. We use, three-dimensional thermo-mechanical numerical models integrating lithospheric and mantle heterogeneities with regional stress conditions to investigate the intraplate seismicity in this region. A crustal seismic velocity model is employed to estimate crustal thickness and density, while seismic velocity anomalies from regional upper-mantle tomography are converted into a temperature field, from which density variations, lithospheric thickness, and rheology are derived. These crustal and mantle heterogeneities are incorporated into numerical models along with far-field east–west compressional stresses. Crustal density and thickness variations are also constrained using Gravitational Potential Energy and Crustal thickness gradients. Models with tomography-based thermal structures with far-field stresses produce localized lithospheric thinning and elevated strain rates that spatially correlate with seismicity. Regions of concentrated seismicity consistently coincide with zones of thinned lithosphere, enhanced strain rate, and positive correlations with gravitational potential energy and crustal thickness gradients. The results indicate that intraplate seismicity in central and southeastern Brazil is controlled by the combined effects of upper-mantle temperature heterogeneity, regional stress, and crustal-scale structural variations. These findings highlight the importance of coupling mantle dynamics with lithospheric and crustal structure to explain earthquake occurrence in intraplate regions.

Keywords: Intraplate Seismicity, Central and Southeastern Brazil, Upper-mantle heterogeneities, Geodynamic Modelling, Gravitational potential energy, Crustal thickness gradient.

1 Introduction

Intraplate earthquakes, though less frequent than those at plate boundaries, remain a fundamental challenge in seismology because they occur far from active tectonic margins and their driving mechanisms are often unclear. Central and southeastern Brazil is among the least studied regions of intraplate seismicity. Although earthquakes in Brazil are relatively less common, they can cause considerable monetary damage and fear among a populace with poor seismic education and a lack of earthquake-resistant structures (Agurto-Detzel et al., 2017). The largest earthquake in this area was the 1955 Porto dos Gaúchos earthquake, with a magnitude of 6.2 (Barros et al., 2009), which is nearly one unit smaller than the largest recorded intraplate earthquake in the world (Schulte & Mooney, 2005). Understanding the processes that control this intraplate seismicity is therefore both a scientific challenge and a societal necessity.

Intraplate seismicity in central and SE Brazil is not uniform, and large areas with relatively no seismicity can be observed (Figure 1). The origin of the seismicity is unclear, with a negligible association with the known tectonic provinces. Earthquake activity in the study area is largely confined to two principal seismic zones: a NE-SW trending zone within the Goiás Massif, and the southern Brasília fold belt, which partly overlaps the São Francisco craton and the northeastern boundary of the Paraná Basin (Assumpção et al., 2004). Earthquakes occur in both fold belts and cratonic areas, which complicates the correlation between earthquake distribution and surface tectonic provinces.

A key tectonic feature in this area is a suture zone (Figure 1b) marking the final collision between the São Francisco Craton and the cratonic block beneath the Paraná Basin. It is well defined by geological mapping and a strong gravimetric gradient (Lesquer, 1981). The suture zone could be a candidate for a weak zone, but seismicity is concentrated only in the southern part, while the northern part remains completely aseismic. This spatial inconsistency suggests that additional factors, beyond mapped tectonic boundaries, play a role in controlling seismic activity.

While local features highlight the complexity of intraplate seismicity in Brazil, there are attempts to identify broader patterns at the continental scale. For instance, seismicity is significantly higher in Neoproterozoic fold belts compared to Phanerozoic basins and old cratonic regions. This trend aligns with their geophysical characteristics, including a thinner lithosphere, elevated heat flow, and reduced elastic thickness. On the other hand, cratonic areas appear comparatively aseismic, which has been attributed to their thick, cold, and mechanically strong lithosphere (Agurto-Detzel et al., 2017). These observations have led to the broader view that earthquake-prone regions correspond to a weaker lithosphere where stresses are preferentially concentrated; however, they do not provide a complete explanation. The interpretations remain largely qualitative, as no direct calculations of stresses were made to confirm that the lithospheric properties on their own can explain the observed seismicity.

While lithospheric properties provide part of the explanation, other studies highlight the importance of upper-mantle structures in controlling intraplate stresses. Lateral variations in the mantle can have a substantial impact on the stress field (Lithgow-Bertelloni & Guynn, 2004). Seismic tomography models reveal significant lateral variations in the upper mantle beneath central and southeastern Brazil. A seismic high-velocity anomaly is identified beneath the São Francisco Craton, with roots extending to depths of 200–250 km (Van Decar et al., 1995; Schimmel et al., 2003). Similarly, high-velocity anomalies have been identified beneath the Paraná Basin, suggesting a buried cratonic nucleus. However, a striking low-velocity cylindrical anomaly in the upper mantle beneath the northeastern Paraná Basin (VanDecar et al., 1995; Schimmel et al., 2003) has been interpreted as a fossil plume conduit, possibly linked to the Tristan da Cunha Plume. At depths of 150–250 km, low-velocity anomalies are concentrated in fold belt areas, correlating with Late Cretaceous igneous provinces (VanDecar et al., 1995; Assumpção et al., 2004). The Tocantins province and Iporá Igneous Provinces, located near the Goiás massif, exhibit strong negative anomalies, potentially associated with the Trindade plume (Gibson et al., 1995, 1997).

Several studies have shown that regions with low-velocity anomalies in the upper mantle align with earthquake clusters, whereas high-velocity zones, like the northern Paraná Basin, exhibit minimal seismicity (Assumpção et al., 2004; Rocha et al., 2011). Although heterogeneities in the lithosphere and upper-mantle are recognized as key factors influencing crustal seismicity, their specific impact on the seismicity of this region has not been thoroughly investigated through large-scale computations of stress field using numerical models.

This study explores how lithospheric and upper-mantle heterogeneities influence intraplate seismicity in the region through 3D geodynamic modeling. Geodynamic simulations provide an effective approach to linking stress sources with crustal seismicity, as they allow for the computation of stress fields considering multiple contributing factors. For instance, numerical models have been used to establish a connection between upper-crustal seismicity and lithospheric as well as upper-mantle heterogeneities in the Korean Peninsula (Lee et al., 2022). Similarly, numerical modelling in the Central and Eastern United States (CEUS) has been employed to link the foundering lithospheric root, as identified through seismic tomography, with modelled parameters such as stress distribution and seismic activity (Becker et al., 2015; Saxena et al., 2021). Building on the modeling approach in other intraplate settings, we apply a similar approach to Brazil. Specifically, we inverted a regional tomography model (Schimmel et al., 2003) to derive a temperature field, which was then used to estimate density and viscosity for the assumed compositions. Far-field tectonic stresses and crustal thickness were also taken into account while simulating the stress state of the region.

In addition to the geodynamic simulations, we created two other independent models to investigate the effect of lateral density contrast of the lithosphere and the crustal thickness variation. We computed the Gravitational Potential Energy (GPE) as a depth-integrated density moment resulting from lateral density variations in the lithosphere. Elevated GPE levels have the potential to drive seismic strain release (Becker et al., 2015). Additionally, crustal thickness variations were also quantified by calculating thickness gradients, which can serve as a potential source of stress (Artyushkov, 1973).

In the subsequent sections, we detail the construction of numerical models to determine the strain field, along with the computation of GPE and crustal thickness variations for the study area (Section 2). After that, the model results are presented, highlighting how strain rate, elevated GPE, and crustal thickness gradients vary spatially across the study area (Section 3). Next, these results are then compared with observed seismicity to evaluate their role in influencing seismic activity. (Section 4). Finally, we address the relative contributions of lithospheric and upper-mantle heterogeneities in shaping the distribution of seismicity of central and southeastern Brazil.

2 Methodology

2.1 Modelling instantaneous mantle flow

2.1.1 Governing equations

The series of 3D numerical models were developed using the open-source code ASPECT Version 2.1.0 (Bangerth et al., 2019; Fraters et al., 2019; Heister et al., 2017; Kronbichler et al., 2012; Rose et al., 2017), which is built on finite element library deal.II 9.0.1(Azetta et al., 2018).The models were built in the framework of mass, momentum and energy conservation, considering Boussinesq approximation, these equations are as follows:

$$-\nabla \cdot \left(2\eta_{eff}\dot{\epsilon}(u)\right) + \nabla P = \rho g \tag{1}$$

$$\nabla \cdot u = 0 \tag{2}$$

$$\rho C_P \left(\frac{\partial T}{\partial t} + u.\nabla T\right) - \nabla.\left(k + v_h(T)\right)\nabla T = 0, \tag{3}$$

where η represents the viscosity (Pa s). The strain rate tensor $\dot{\epsilon}(u)$ is expressed as: $\dot{\epsilon}(u) = \frac{1}{2}(\nabla u + (\nabla u)^T)$. The velocity field is denoted by u (m s^{-2}), and the pressure field is represented by P (Pa). ρ (kg m^{-3}) represents the density, g is the gravitational acceleration (m s^{-2}), The thermal evolution is governed by temperature T (K), heat capacity C_p (J kg^{-1} K^{-1}), thermal conductivity κ (W m^{-1} K^{-1}), and time t (s).

Since multiple compositional fields are used, a Discontinuous-Galerkin method (He et al., 2017) The system also includes is implemented in ASPECT for the advection of compositional fields C_i influenced by source terms q_i, given by:

$$\frac{\partial C_i}{\partial t} + u \cdot \nabla C_i = q_i \tag{4}$$

2.1.2 Constitutive nonlinear rheology

We used ASPECT to model lithospheric deformation and compute the strain rates due to instantaneous mantle flow, which is known to have an important baring on the distribution of earthquakes in stable cratons (Lee et al., 2022, Saxena et al., 2021). To implement effect of material properties of both lithosphere and mantle on earthquake distribution, we employed a visco-plastic rheology as material model in ASPECT. This model rheology depends primarily on diffusion-dislocation creep laws and the Drucker-Prager criterion, which can be combined with various complex rheological factors. At higher temperatures, materials experience nonlinear viscous deformation via power-law dislocation creep or grain boundary (or bulk) diffusion creep. These two rheologies can be expressed by strain rate and temperature-dependent viscosity as:

$$\eta_{eff}^{vis} = \frac{1}{2} A^{\frac{-1}{n}} d^{\frac{m}{n}} \dot{\epsilon}_{ii}^{\frac{(1-n)}{n}} exp\left(\frac{E+PV}{nRT}\right) \tag{5}$$

where A is the prefactor, n is the stress exponent, $\dot{\epsilon}_{ii} = \sqrt{\frac{1}{2}\dot{\epsilon}'_{ij}\dot{\epsilon}'_{ij}}$ is the effective deviatoric strain rate, which is the square root of second invariant of deviatoric strain rate tensor, *d* is the grain size, *m* is the grain size exponent, *E* is the activation energy, *V* is the activation volume and *R* is the gas constant. In case of diffusion creep η_{eff}^{df}, n =1 and m > 0, while for dislocation creep (η_{eff}^{dl}) *n*>1 and *m*=0.

At relatively low temperatures the material behavior is modelled using plastic rheology. The effective viscosity is locally adopted so that the stress generated during deformation does not exceed the yield stress (viscosity rescaling method). The effective plastic viscosity is given by

$$\eta_{eff}^{pl} = \frac{\sigma_y}{2\dot{\epsilon}_{ii}} \tag{6}$$

where σ_y is the yield stress. Here, plasticity limits the viscous stress via Drucker-Prager yield criterion given by:

$$\sigma_y = Ccos(\varphi) + Psin(\varphi) \tag{7}$$

where C is the cohesion and φ is the friction angle.

In geological conditions, under the same deviatoric stress, both the viscous creep processes act simultaneously. We thus consider composite viscous rheology by harmonically averaging μ_{eff}^{dl} and μ_{eff}^{df}.

$$\eta_{eff}^{cp} = \frac{\eta_{eff}^{df}\eta_{eff}^{dl}}{\eta_{eff}^{df} + \eta_{eff}^{dl}} \tag{8}$$

Moreover, the viscous creep and plastic yielding are assumed to be independent simultaneously occurring processes, and the lowest effective viscoplastic stress resulting from this mechanism is favoured, which is expressed as,

$$\eta_{eff}^{vp} = min\left(\eta_{eff}^{pl}, \eta_{eff}^{cp}\right) \tag{9}$$

Strain weakening is included in the system by calculating the finite strain invariant through compositional fields within the material model and linearly reducing the cohesion and internal friction angle as a function of the finite strain magnitude. While calculating the finite strain invariant (e_{ii}), a single composition field tracks the value of finite strain invariant via

$$e_{ii}^{t} = e_{ii}^{(t-1)} + \dot{e}_{ii}dt \tag{10}$$

where *t* and *t-1* are current and prior time steps, $\dot{e}_{ii}$ is the second invariant of the strain rate tensor, and *dt* is the time step size. When the accumulated strain is less than a given value, *C* and *φ* are constant. For accumulated strain values greater than this threshold, *C* and *φ* decrease linearly until the system reaches a certain maxima of accumulated strain, after which they are kept constant again. The effective viscosity is calculated by taking a harmonic average of the viscosities derived from diffusion and dislocation creep, accounting for plastic yielding.

2.1.3 Model Parameters

The model geometry is defined as a 3D spherical shell with dimensions of 38°– 57°W, 12°–30°S, and 0– 660 km. The whole numerical domain is discretized into 0.25° × 0.25° × 10 km, and the top 50 km are further refined to 0.125° × 0.125° × 5 km such that the crustal thickness variations are sufficiently resolved. (Figure 2a)

The model domain is comprised of three layers: upper crust, lower crust, and mantle. The upper and lower crustal thicknesses and densities are taken from the CRUST1.0 model (Laske, 2013; Figure 3). The upper crustal density is set to 2626 kg m^{-3}, representing the thickness-weighted average of water, sediment, and upper crust. The lower crust density is 3247 kg m^{-3}, derived from the thickness-weighted average of middle and lower crust densities from the CRUST 1.0 model. The rheological parameters and equation of state for various lithologies included in the model are derived from previous studies (Table 1). For the upper crust, lower crust, and mantle, laboratory-derived viscous flow laws of wet quartzite, wet anorthite, and dry olivine are used, respectively. For the mantle, a volumetric thermal expansivity (α) of $3 \times 10^{-5}\, K^{-1}$ is taken, but a value of zero is assigned to the crust, discarding the thermal buoyancy effects within the crust.

The initial temperature profile is inferred from seismic velocity anomalies obtained from tomographic data following (Goes et al, 2000). First, we obtain temperature derivative of the *P*- and *S*-waves from the following expressions:

$$\frac{\partial V_p}{\partial T} = \frac{1}{2\sqrt{\rho}} \frac{1}{\sqrt{K + \frac{4}{3}G}} \frac{\partial\left(K + \frac{4}{3}G\right)}{\partial T} - \frac{\sqrt{K + \frac{4}{3}G}}{2\rho^{1.5}} \frac{\partial \rho}{\partial T} + Q_p^{-1} \frac{aE}{2RT^2 \tan\frac{\pi a}{2}} \qquad (11)$$

$$\frac{\partial V_s}{\partial T} = \frac{1}{2\sqrt{\rho}} \frac{1}{\sqrt{G}} \frac{\partial G}{\partial T} - \frac{\sqrt{G}}{2\rho^{1.5}} \frac{\partial \rho}{\partial T} + Q_s^{-1} \frac{aE}{2RT^2 \tan\frac{\pi a}{2}} \qquad (12)$$

where K is the bulk modulus, G is the shear modulus, ρ is density, Q_p and Q_s are the quality factors for the P- and S-waves respectively, a is an exponent defining the frequency dependence of the attenuation, E is the activation energy, and R is the gas constant. On the right-hand side of equations (1) and (2), the first and second terms are relevant to elasticity, while the other is relevant to anelasticity. To obtain temperature anomalies from observed seismic velocities, we then use equations (1) and (2) to iteratively minimized the residual function,

$$R = \left(\frac{\partial V}{\partial T}\right)_{elastic} + \left(\frac{\partial V}{\partial T}\right)_{anelastic} - \left(\frac{\partial V}{\partial T}\right)_{observed} \tag{13}$$

using a Newton-Raphson scheme. This approach provides an estimate of the subsurface thermal structure consistent with both elastic and anelastic effects. In this study, a regional tomography model was used to calculate temperature anomalies (Schimmel et al. 2003); we only inverted the P-wave velocity perturbations due to better resolution in the model. The temperature inversion was done for our model domain, focusing on the study area [12°–30°S, 38°–57°W, and 0–660 km]. Figure 4 shows the P-wave velocity anomalies (Schimmel et al. 2003) and the inverted temperature anomalies beneath the study area. As this study focuses on correlating the seismicity of Brazil, we masked the oceanic region (black-shaded area; Figure 4) to emphasize the heterogeneous nature of the continental subsurface. The details of the procedure are provided in Appendix A.

Free-slip (tangential) velocity boundary conditions are assumed in the bottom boundary and most of the side walls. The top boundary is modelled as a free surface to accommodate any topographic change caused by the traction within our domain (Rose et al., 2017) (Figure 2b). In practice, several numerical time steps are required for an initially flat top surface to reach a quasi-isostatic state, as it deforms in response to vertical tractions within ASPECT's Arbitrary Lagrangian-Eulerian framework (Rose et al., 2017). The temperature is set to 273 K on this boundary. Traction boundary conditions are applied to the lithospheric section of the western sidewall while the remaining boundaries remain open (Figure 2b). The magnitude of the traction is taken as 30 MPa, as it corresponds with previous studies (Assumpção & Sacek, 2013). This boundary condition is appropriate because Brazil is characterized by mostly east-west compression (Coblentz & Richardson, 1996).

Four models were constructed (Table 2) to investigate the effects of heterogeneities in the crust and upper mantle, as well as the influence of far-field tectonic stresses. The models are denoted as model a-b (a = 1 or 2, and b = 1 or 2). Models 1-b have variations in crustal thickness, but the mantle temperatures are taken as an averaged reference geotherm (Turcotte & Schubert, 2014), instead of a tomography-based temperature field. Models 2-b consist of a tomography-based temperature field, unlike models 1-b. The second index in the model label indicates one of the two traction boundary conditions. In models a-1, all the side boundaries have free-slip boundary conditions, while the top boundary remains a free surface. Models a-2 differ from model a-1 in that they have a traction boundary condition in the western side wall of a magnitude of 30 MPa.

2.2 Computing gravitational potential energy (GPE) distribution

Lateral variations in lithospheric density and thickness generates differences in gravitational potential energy (GPE), which act as a significant source of horizontal stresses within continental interiors (Barrows & Langer, 1981; Neres et al., 2018). In our model domain, the GPE per unit area is determined using the thin-sheet approximation (Ghosh et al. 2009):

$$GPE = \int_{-h}^{L} z\rho(z) g dz \tag{14}$$

where, $\rho(z)$ is the density at depth z, h is the topography and L is the assumed compensation depth. The compensation depth has been chosen at a depth of 200 km. This depth represents the approximate thickness of the lithosphere for the continents (McKenzie et al., 2005). The crustal density and thickness distribution are taken from the LITHO1.0 model (Pasyanos et al., 2014). To model the elevated GPE distribution, a standard reference is calculated using the average thicknesses and densities of the crustal layers.

The GPE model, which is based on LITHO 1.0's crustal density model, lacks isostatic equilibrium, which may indicate significant mantle flow support or lithospheric compensation (Becker et al., 2015). To address this, we develop a compensated GPE model (GPE_c) by enforcing isostatic balance at specific depths, allowing for variable density anomalies in the mantle lithosphere.

2.3 Calculating crustal thickness gradient

To analyze the spatial variations in crustal structure, we compute the gradient of the crustal thickness field using the data from LITHO 1.0 (Pasyanos et al., 2014). As the dataset is discrete, the gradient is approximated using finite differences:

$$\frac{\partial f}{\partial x} \approx \frac{f(x+\Delta x, y) - f(x-\Delta x, y)}{2\Delta x} \tag{15}$$

$$\frac{\partial f}{\partial y} \approx \frac{f(x, y+\Delta y) - f(x,\ y-\Delta y)}{2\Delta y} \tag{16}$$

Where $f(x,y)$ represents the crustal thickness at coordinates (x,y), Δx and Δy represent small changes in longitude and latitude, respectively. The gradient magnitude is given by:

$$|\nabla f| = \sqrt{\left(\frac{\partial f}{\partial x}\right)^2 + \left(\frac{\partial f}{\partial y}\right)^2} \tag{17}$$

The continent-ocean transition zone is expected to exhibit a strong regional crustal thickness gradient in the region. As a result, an overall comparison with the observed seismicity is difficult to achieve, but investigating the variations of crustal thickness in the continental part of Brazil might provide valuable insights into the crustal stability of the region. To highlight variations within the continent, we only compute gradient magnitudes for the continental part of Brazil, covering 57°W–45°W and 23°S–12°S.

2.4 Quantification of the prediction power of modelled quantities

To evaluate how well the model-derived quantities capture the spatial patterns of seismicity in central and southeastern Brazil, we employed Molchan curves (Molchan, 1990, 1991; Molchan & Kagan, 1992) and their associated skill values (Becker et al., 2015; Saxena et al., 2021). Molchan analysis provides a standardized framework to assess the predictive power of a given geodynamic quantity (hereafter referred to as a predictor) in relation to the observed earthquake distribution.

Each predictor was normalized using a min–max scaling, and subsequently expressed as a fraction of space under "alarm", defined as the portion of the study region where the predictor value is less than or equal to a given threshold. For every threshold, the fraction of earthquakes occurring outside the occupied space was calculated and defined as the fraction of missed earthquakes. A Molchan curve is then constructed by plotting the fraction of missed earthquakes against the corresponding fraction of space under alarm. Molchan curves are bounded by $\{0,1\}$ and $\{1,0\}$, corresponding to the cases where no space is under alarm and all earthquakes are missed, and where the full space is under alarm and no earthquakes are missed, respectively.

The predictive skill, S of a Molchan curve is obtained by subtracting 0.5 from the area above the Molchan curve (Becker et al., 2015). A purely random predictor yields S=0, a perfect correlation yields S=0.5, and a perfect anti-correlation yields S=−0.5. In practice, larger magnitudes of S indicate stronger spatial correlation between the predictor and seismicity.

This framework allows for direct comparison of the predictive capacity of different model-derived quantities and highlights which parameters are most closely linked to the spatial distribution of earthquakes in our study area.

3 Results

3.1 Temperature structures

Two distinct temperature configurations emerge in Models 1s and 2s. Model 1s exhibits a predominantly one-dimensional geotherm, with temperature increasing smoothly with depth. To examine these structures more closely, we extracted two vertical transects at 13°S and 20°S. Both sections reveal laterally uniform thermal gradients, consistent with a spatially homogeneous lithospheric structure (Figure 5a). The inferred lithospheric thickness is similarly uniform along both transects, with an average thickness of approximately 130 km (Figure 5a). We set the 1300 K isotherm as a conceptual lithosphere-aesthenosphere boundary. In contrast, Model 2s displays a tomography-inverted, fully three-dimensional temperature field characterized by pronounced lateral thermal heterogeneity. Along the 13° S transect, a distinct plume-like thermal anomaly is evident within the mantle, accompanied by significant lithospheric thinning directly above the plume head (Figure 5b). At 20° S, additional high-temperature mantle bodies are present, and the lithospheric thickness varies laterally along the section (Figure 5b). These features collectively indicate strong lateral variations in mantle temperature and lithospheric structure in Model 2s. In the tomography-inverted models (2s), the lithospheric thickness ranges from 68 to 139 km, reflecting the underlying temperature structure. The spatial distribution of seismicity shows a strong connection to these thermal variations in Model 2s. The earthquake clusters tend to occur directly above regions where the lithosphere is thinned, particularly above the plume-related thermal anomalies (Figure 5b).

3.2 Strain rate distribution

We computed velocities and strain rates that are in equilibrium with the buoyancy forces arising from the instantaneous mantle flow in our numerical model (section 2.1). The strain rate distribution at the surface for model 1s did not show any correlation with observed seismicity (Figure 6(a-b)). In model 1-1, the overall magnitude of the strain rate is small, and the distribution is diffused in nature (Figure 6a). There is a region of high strain rate right over Paraná Basin but there's not much notable seismicity recorded at that region, where as zones of low strain rates are observed near RB and left of BB. In model 1-2, the overall magnitude of the strain rate is higher than that of model 1-1 (Figure 6b). There is a high strain rate band observed vertically along 54°W longitude. Despite this apparent localization, the strain-rate pattern does not align with any major seismogenic zones, and earthquake epicenters remain largely dispersed outside the predicted high strain-rate band.

In model 2s, where a tomography-based temperature distribution had been implemented, much complicated strain rate patterns are observed than the previous two models (model 1s). For model 2-1, several places with particularly higher strain rate bands are observed (Figure 6c). In the northern part of the domain two thin curved bands are present near the Goiás Massif. A broad region of high strain rate is also present along the southern margin of Brazil, and another zone of moderate to high strain rate occurs within the Paraná Basin. Notably, the high strain-rate regions near the Goiás Massif and southern Brazil spatially coincide with clusters of intraplate earthquakes, indicating a clear correspondence between modelled deformation and observed seismicity. In model 2-2, where the effect of far-field compression had been considered, the average strain rate magnitude is higher than that of model 2-1. Two thick high strain rate bands are observed, one is trending NE-SW near Goiás Massif, another is trending NW-SE, went through the Paraná Basin and RB. Another zone of high strain rate is present in between RB and AB. There are also zones of low strain rates present. One is located in BB and western part of São Francisco Craton, others are at the southern part of AB, and at the south-western part of the Paraná Basin (Figure 6d). The NE-SW and NW-SE bands closely correspond to the primary seismic belts observed across continental Brazil, providing the strongest spatial agreement between modelled strain rates and earthquake distributions among all tested models. Within the NW-SE band, seismicity is concentrated primarily in its southern segment, whereas the northern portion remains largely aseismic, indicating that strain localization alone may not be sufficient for earthquake occurrence. The smaller band between RB and AB shows only weak correspondence with seismicity, suggesting the influence of additional lithospheric or rheological controls.

The Molchan skill scores for model 1-1 and model 1-2 are -0.118 and -0.016 (Figure 9a). In contrast, model 2-1 and 2-2 yield positive values of 0.065 and 0.137 (Figure 9a).

3.3 Gravitational potential energy (GPE) distribution and Crustal thickness variations

The distribution of gravitational potential energy in the study area is uneven, with some regions showing elevated GPE values. Others showing a decrease, and some maintaining normal levels (Figure 7a). Elevated GPE values are concentrated in the regions of GM, BB, the northern part of the São Francisco Craton, eastern Paraná Basin, south of Amazon craton, and the southern part of RB. In contrast, recessed GPE values are observed in the central Paraná Basin, the southern part of São Francisco Craton, northern RB, and AB. In the compensated GPE model, the regions with elevated GPE values appear more diffused compared to the uncompensated GPE model (Figure 7b). The high GPE value regions are located at similar locations as the uncompensated model. The Very high GPE values near

Goiás Massif, that are observed in the uncompensated GPE model are not present in the compensated model. The elevated GPE distribution yielded a Molchan skill of 0.079, while the compensated GPE model (GPE_c) produced a value of 0.090 (Figure 9b).

The crustal thickness gradient for the continental part of the Brazil has been calculated. The distribution is uneven, with some areas showing higher variations in crustal thickness than the others, ranging from 0 to 5 km/° (Figure 8). Near the Goiás Massif, a patchy NE-SW trending zone of high gradient values are present. Several patches of strong gradients are observed in the Paraná Basin, São Francisco Craton, and Amazon Craton.

4 Discussion

4.1 Analysis of the results

The four numerical models investigated here revealed how the upper-mantle thermal anomalies and far-field tectonic stress influence the present-day instantaneous mantle flow vis-à-vis the intraplate deformation field in Brazil and its correspondence with seismicity. Our simulations show that temperature field exerts a first-order control on the model behaviour. The contrasting behaviour of Models 1s and 2s highlights the central role of lithospheric and mantle temperature structure in shaping surface deformation patterns. The laterally variable temperature field in Model 2s leads to a heterogeneous lithospheric thickness. This thickness variation creates a lateral viscosity gradient which strongly influences how stresses are distributed across the domain (Mooney et al., 2012). Thermally eroded regions are marked by lithospheric thinning and are correlated with elevated strain rates that reflect a mechanically weakened column (Figure 5b) and enhanced sensitivity to imposed boundary forces (Tesauro et al., 2015). These zones of concentrated deformation also coincide with the locations of mapped earthquake clusters (Figure 5b), indicating that lithospheric thinning not only governs the spatial partitioning of strain but may directly influence the location of enhanced seismic failure-rates. A similar association between seismicity and lithospheric thinning has been reported by multiple studies in other stable continental regions (Craig et al., 2011; Mazzotti 2007; Mooney et al., 2012; Sloan et al., 2011). The Molchan skill scores support this interpretation: the uniform-temperature models (1s) yield negative or near-zero values, confirming the absence of meaningful spatial correspondence with seismicity, whereas the tomography-inverted models (2s) produce positive skill scores (Figure 9a). This improved skill demonstrates that the heterogeneous temperature induced lithospheric thinning, is essential for reproducing the non-random spatial pattern of earthquakes in Brazil craton. Differences between the paired simulations (1-1 vs. 1-2; 2-1 vs. 2-2) further show that traction boundary conditions modulate these deformation patterns (Figure 6). Under identical thermal structures, variations in applied traction redistribute stress and strain within the lithosphere, but the magnitude and geometry of this redistribution are still fundamentally controlled by the underlying temperature structure. The introduction of traction further increases the Molchan skill (Figure 9a), indicating that boundary forcing enhances the spatial alignment between strain localization and earthquake occurrence when the underlying thermal structure already predisposes the lithosphere to deformation.

The gravitational potential energy (GPE) distribution in the study area exhibits several notable correlations with the observed earthquake patterns (Figure 1b, 7). Lateral density variations in the lithosphere elevate GPE and generate horizontal gravitational stresses, providing a potential source of intraplate deformation (Barrows & Langer, 1981; Becker et al., 2015; Neres et al., 2018; Schmalholz et al., 2014). In Brazil, elevated GPE values in the Goiás Massif, the northern São Francisco Craton, and the region southern Brazil coincide with clustered seismicity, consistent with the idea that regions of enhanced lateral density contrasts can promote stress accumulation and favor intraplate earthquake occurrence.

Conversely, the low GPE values across the central Paraná Basin correspond with its comparatively low seismicity (Figure 1b, 7), suggesting a weaker gravitational driving force. Similar influence on seismicity has been demonstrated in central and eastern United States (Becker et al., 2015; Saxena et al., 2021). Some mismatches do occur: the Brasília Fold Belt shows high GPE yet remains largely aseismic, whereas the southern São Francisco Craton hosts a prominent seismic cluster despite relatively low GPE, indicating that GPE alone does not fully dictate the spatial pattern of seismicity. The compensated GPE model enhances the amplitude of lateral GPE variations relative to the uncompensated case, but the overall pattern remains similar (Figure 7). Both models yield positive Molchan skill scores, with the compensated model (0.090) outperforming the uncompensated one (0.079) (Figure 9b), demonstrating that GPE provides meaningful, non-random predictive power for the spatial distribution of intraplate earthquakes.

To assess the statistical significance of the skill scores, we establish a lower bound of correlation using Monte Carlo simulations based on purely random spatial fields (Becker er al., 2015). We generated 1000 samples of random numbers (between zero and one) over the study region to quantify the minimum level of non-random spatial correlation. The maximum skill value obtained from these simulations is 0.071, which we take as the lower bound of non-randomness. Also, a Molchan analysis of seismic moment distribution, a quantity that inherently correlated with the earthquake distribution, yielded aa skill score of 0.428. This provides a realistic upper bound for meaningful predictive performance (Becker et al., 2015; Lee et al., 2022). Accordingly, the Molchan skill scores of models 1-1, 1-2, and 2-1 fall below the lower bound of 0.071, indicating no meaningful correlation with the observed earthquake distribution. In contrast, model 2-2 attains a skill score of 0.137, exceeding the non-randomness threshold and representing the strongest spatial correspondence with seismicity among all the models. This indicates that the combination of heterogeneous upper-mantle structure and imposed far-field tectonic compression provides a more realistic representation of the regional stress field, thereby offering a better explanation for the observed seismicity. The GPE-based predictors also yield skill scores >0.071, indicating positive correlations with the earthquake distribution, with the compensated model performing better. This improvement reflects that enforcing isostatic balance introduces mantle-lithospheric density contributions, producing a more physically consistent GPE field that better captures regional stress patterns.

Next, we focus on the two most prominent seismic belts in the region: the NE–SW band across the Goiás Massif and the NW–SE band of earthquakes along the major suture zone (Assumpção et al., 2004). For model-derived quantities, we restrict our analysis to model 2-2, which demonstrates that dynamic support is essential and yields the highest Molchan skill score among the tested models (Figure 9a). The GPE distributions are also incorporated to evaluate their contribution to the observed deformation patterns. In addition, we examine the crustal thickness gradient field, computed only for the continental portion of Brazil. Although we do not attempt a direct regional correlation between crustal thickness gradients and seismicity, given that the continent-ocean transition could obscure the overarching pattern. Instead, we use the results to assess variations of crustal thickness within the two focused regions. These variations offer further insight into the potential controls on crustal stability and lithospheric structure.

4.2 Seismicity in the Goiás Massif

The Goiás Massif represents one of the most prominent intraplate seismic belts in the study region, characterized by a well-defined NE–SW–trending band of earthquake clusters (Assumpção et al., 2004; Rocha et al., 2014) (Figure 1b). Our results indicate that this seismicity cannot be attributed to a single controlling factor; rather, it emerges from the combined influence of thermal, mechanical, and compositional heterogeneities within the lithosphere–mantle system. In model 2-2, the Goiás Massif is underlain by a pronounced upper-mantle high-temperature anomaly (Feng et al., 2007; Rocha et al., 2011; Schimmel et al., 2003) that is absent in the laterally uniform temperature models. This anomaly induces localized lithospheric thinning, resulting in a mechanically weakened lithospheric column (Figure 5b). The reduced strength enhances the lithosphere's sensitivity to both buoyancy-driven stresses and imposed far-field tractions owing to the subduction of Nazca plate beneath South Americal plate (Araújo de Azevedo et al., 2015; Rocha et al., 2011). Consistent with this framework, the modeled strain-rate field displays a distinct NE–SW-trending band of elevated strain rates that spatially coincides with the observed seismicity belt across the Goiás Massif, indicating preferential localization of deformation within the thinned lithosphere.

The gravitational potential energy (GPE) distribution further supports this interpretation (Figure 7). The Goiás Massif is associated with elevated GPE values in both uncompensated and compensated models, indicating the presence of significant lateral density contrasts within the lithosphere. These contrasts generate horizontal gravitational stresses that can contribute to intraplate deformation (Becker et al., 2015; Jones et al., 1996). While elevated GPE alone does not guarantee seismicity, as evidenced by aseismic high-GPE regions elsewhere, it likely acts as an important source of background stress that amplifies deformation when combined with lithospheric weakening.

The Goiás Massif is also characterized by strong lateral gradients in crustal thickness, forming patchy NE–SW–trending zones that broadly coincide with the observed seismicity band (Figure 8). These lateral Variations in the crustal thickness can lead to differential stress accumulation (Artyushkov 1973). Such differential stresses can locally enhance the likelihood of brittle failure when combined with elevated strain rates and reduced lithospheric strength.

All these results emphasizes that seismicity in this region is a combined effect of upper-mantle thermal anomalies, far-field stress, lithospheric thinning, elevated strain rates, high GPE, and strong crustal thickness gradients, which creates a mechanically favorable environment for stress localization and release.

4.3 Seismicity in the suture zone

The suture zone represents a major inherited lithospheric structure within the study area (Lesquer et al., 1981) (Figure 1b). In model 2-2, the surface strain-rate field exhibits a pronounced NW–SE–trending band of elevated strain rates that closely follows the mapped trace of the suture zone. Despite this continuous strain localization, observed seismicity is confined to the southeastern segment of the suture, whereas the northern segment remains largely aseismic (Assumpção et al., 2004) (Figure 1b). This spatial discrepancy indicates that elevated strain rate alone does not dictate earthquake occurrence.

The strain-rate pattern reflects the integrated response of the lithosphere to mantle temperature structure and boundary forcing, establishing a background state of stress accumulation along the suture. The GPE distribution shows moderately elevated values along the suture zone, with slightly higher magnitudes in the compensated model. However, the GPE field does not exhibit strong along-strike variations that would explain the contrast between the seismically active southern segment and the aseismic northern segment, suggesting that GPE provides a regional stress contribution but solely does not control seismic segmentation.

A clear distinction emerges from the crustal thickness gradient field. The southeastern segment of the suture zone is characterized by pronounced crustal thickness gradients, whereas the northern segment shows weak or negligible gradients (Figure 8). The pronounced lateral gradients in crustal thickness introduce strong horizontal gravitational stresses, enhancing differential stress accumulation within the crust which led to the intraplate seismicity in this region (Artyushkov 1973; Gao et al., 2020).

Taken together, these observations suggest a two-stage control on seismicity along the suture zone. Mantle temperature structure and associated lithospheric weakening establish a background state of elevated strain accumulation along the entire suture. However, the release of this strain as earthquakes appears to be modulated by crustal-scale heterogeneities, particularly variations in crustal thickness. Where such heterogeneities are strong, as in the southeastern segment, seismicity is promoted; where they are weak, as in the northern segment, the suture remains largely aseismic. The combined effects of mantle-driven deformation and crustal structure provide a consistent explanation for the segmented pattern of seismicity along the suture zone.

4.4 Limitations

The numerical models presented in this study are intended to capture first-order controls on intraplate deformation and seismicity at lithospheric scales and therefore necessarily involve simplifying assumptions. The simulations focus on temperature-driven density and viscosity variations inferred from seismic tomography and do not explicitly account for lateral chemical heterogeneities in the mantle. Such compositional variations may locally influence the inferred temperature field and associated buoyancy forces, although the large-scale thermal patterns employed here are expected to represent the dominant controls on regional deformation. In addition, the models represent steady-state deformation and do not resolve transient elastic effects or fault-scale processes.

5 Conclusion

In this study, we investigated the controls on intraplate seismicity in Central and Southeastern Brazil using three-dimensional thermo-mechanical numerical models constrained by lithospheric and mantle temperature structure, gravitational potential energy, and crustal thickness variations. We inverted a regional tomography data to invert for the temperature field from which corresponding density and lithospheric structure were derived and implemented in a suite of numerical models to assess roles of mantle temperature heterogeneity and far-field tectonic tractions. To further constrain crustal-scale contributions, we modeled gravitational potential energy and crustal thickness gradients across the study region, allowing us to evaluate their influence on the present-day deformation and seismicity patterns. Our results show that laterally homogenous temperature models fail to reproduce observed seismicity patterns, whereas tomography-based temperature structures produced localized lithospheric thinning, elevated strain rate, and positive Molchan skill scores. Regions of concentrated seismicity consistently coincide with thinned lithosphere and elevated strain rate regions. The results indicate that intraplate seismicity is not controlled by any single factor. Mantle temperature structure establishes a background state of lithospheric weakening and strain accumulation, while gravitational potential energy and boundary tractions contribute regional stresses. Crustal-scale heterogeneities, particularly variations in crustal thickness, modulate where this strain is ultimately released as earthquakes. This study represents the first large-scale numerical modeling effort to directly link lithospheric and upper-mantle heterogeneities with intraplate seismicity in Brazil. By integrating geophysical observations with thermo-mechanical modeling, the results provide new insight into how mantle processes, lithospheric weakening, and crustal structural variations jointly influence earthquake occurrence in regions lacking clear plate-boundary control. Future work can build on this framework by incorporating additional geological and geodynamical constraints and by extending the approach to other intraplate regions, thereby improving seismic hazard assessments in tectonically stable settings.

6 Acknowledgements

The present work has been supported by the Indian Institute of Technology Gandhinagar and an INSPIRE faculty fellowship (DST/INSPIRE/04/2022/002647) granted by Department of Science and Technology (DST), India to DG. We thank the Computational Infrastructure for Geodynamics (geodynamics.org), which is funded by the National Science Foundation under award EAR-0949446 and EAR-1550901 for supporting the development of ASPECT. The figures are made using ParaView v5.8.1, PyGMT v0.11.0 (Tian et al., 2024; Wessel et al., 2019), and Matplotlib v3.10.0.

7 Declaration of interest

The authors declare that they have no known competing financial interests or personal relationships that could have appeared to influence the work reported in this paper.

Appendix A

A.1 Inferring temperatures from seismic velocity anomalies

Determining temperatures from seismic wave velocities is a key step in our modelling approach, as temperature will influence both the driving force and viscous resistance in our geodynamic models. We follow the approach of Goes et al. (2000) for inverting seismic velocity anomalies, taking the derivatives of *P*- and *S*-wave velocities (V_p and V_S, respectively) with respect to temperature (T), where both the effects of elasticity and anelasticity were considered. The expressions for the temperature derivative of the *P*- and *S*-waves are as follows:

$$\frac{\partial V_p}{\partial T} = \frac{1}{2\sqrt{\rho}}\frac{1}{\sqrt{K+\frac{4}{3}G}}\frac{\partial\left(K+\frac{4}{3}G\right)}{\partial T} - \frac{\sqrt{K+\frac{4}{3}G}}{2\rho^{1.5}}\frac{\partial\rho}{\partial T} + Q_p^{-1}\frac{aE}{2RT^2\tan\frac{\pi a}{2}} \tag{1}$$

$$\frac{\partial V_s}{\partial T} = \frac{1}{2\sqrt{\rho}}\frac{1}{\sqrt{G}}\frac{\partial G}{\partial T} - \frac{\sqrt{G}}{2\rho^{1.5}}\frac{\partial\rho}{\partial T} + Q_s^{-1}\frac{aE}{2RT^2\tan\frac{\pi a}{2}} \tag{2}$$

where K is the bulk modulus, G is the shear modulus, ρ is density, Q_p and Q_s are the quality factors for the P- and S-waves respectively, a is an exponent defining the frequency dependence of the attenuation, E is the activation energy, and R is the gas constant. On the right-hand side of equations (1) and (2), the first and second terms are relevant to elasticity, while the other is relevant to anelasticity. Again, following Goes et al. (2000), the quality factors are expressed as:

$$Q_p^{-1} = \left(1-\frac{4}{3}\left(\frac{V_s}{V_p}\right)^2\right)Q_k^{-1} + \frac{4}{3}\left(\frac{V_s}{V_p}\right)^2\left(A\omega^a exp\left(\frac{a(E+PV)}{RT}\right)\right)^{-1} \tag{3}$$

$$Q_s^{-1} = \left(A\omega^a exp\left(\frac{a(E+PV)}{RT}\right)\right)^{-1} \tag{4}$$

where Q_k is the bulk attenuation constant. A is the scaling factor, ω is the seismic frequency, P is the pressure, and V is the activation volume.

The elastic terms in equations (1) and (2) were evaluated based on the mantle xenoliths found in Brazil. The anelastic term was evaluated with parameters for olivine, which is a major constituent mineral of the upper mantle. The xenoliths found in Brazil are mostly consist of sp-Peridotites (Fernandes et al., 2021). The constituent minerals include Olivine (Ol), Orthopyroxene (Opx), Clinopyroxene (Cpx), and spinel (Sp). A different composition was taken for the uppermost 100 km (Frost, 2008), the constituent minerals and their proportions are olivine (56%), orthopyroxene (24%), clinopyroxene (12%), plagioclase (10%), and garnet (2%). For the rest of the mantle, we used the following mineral proportions: olivine (72%), orthopyroxene (10%), clinopyroxene (15%), and spinel (3%) (Fernandes et al., 2021). The details of the various elastic parameters of the relevant minerals are provided in Table A1. The anelastic parameters for olivine are given as: $A = 1.48 \times 10^{-1}$, $E = 500 \times 10^3\ J\,mol^{-1}$, $V = 20 \times 10^{-6} m^3 mol^{-1}$, $a = 0.15$, $= 8.314\,Jk^{-1}mol^{-1}$ and $\omega = 1\ Hz$ (Goes et al. 2000).

To obtain temperature anomalies from observed seismic velocities, we iteratively minimized the residual function,

$$R = \left(\frac{\partial V}{\partial T}\right)_{elastic} + \left(\frac{\partial V}{\partial T}\right)_{anelastic} - \left(\frac{\partial V}{\partial T}\right)_{observed} \tag{5}$$

using a Newton-Raphson scheme. This approach provides an estimate of the subsurface thermal structure consistent with both elastic and anelastic effects. In this study, a regional tomography model was used to calculate temperature anomalies (Schimmel et al. 2003); we only inverted the P-wave velocity perturbations due to better resolution in the model. The temperature inversion was done for our model domain, focusing on the study area [12°–30°S, 38°–57°W, and 0–660 km]. An average geotherm of the continental and oceanic upper mantle (Turcotte & Schubert, 2002) was added to the obtained temperature anomalies. This temperature field is used as an input for the numerical model presented later. The inversion script was adapted from Lee (2020). Building on it, we performed the inversion with two distinct compositions (mineral proportions) in the model domain, i.e., the top 100 km and from 100 to 660 km, to distinguish the mineralogical differences between the lithosphere and the upper mantle as much as possible.

References

Agurto-Detzel, H., Assumpção, M., Bianchi, M., & Pirchiner, M. (2017). Intraplate seismicity in mid-plate South America: Correlations with geophysical lithospheric parameters. Geological Society, London, Special Publications, 432(1), 73–90. https://doi.org/10.1144/SP432.5

Alzetta, G., Arndt, D., Bangerth, W., Boddu, V., Brands, B., Davydov, D., Gassmöller, R., Heister, T., Heltai, L., Kormann, K., Kronbichler, M., Maier, M., Pelteret, J.-P., Turcksin, B., & Wells, D. (2018). The deal.II library, version 9.0. Journal of Numerical Mathematics, 26(4), 173–183. https://doi.org/10.1515/jnma-2018-0054

Araújo de Azevedo, P., Rocha, M. P., Soares, J. E. P., & Fuck, R. A. (2015). Thin lithosphere between the Amazonian and São Francisco cratons in central Brazil revealed by seismic P-wave tomography. Geophysical Journal International, 201(1), 61–69. https://doi.org/10.1093/gji/ggv003

Artyushkov, E. V. (1973). Stresses in the lithosphere caused by crustal thickness inhomogeneities. Journal of Geophysical Research, 78(32), 7675–7708. https://doi.org/10.1029/JB078i032p07675

Assumpção, M., An, M., Bianchi, M., França, G. S. L., Rocha, M., Barbosa, J. R., & Berrocal, J. (2004). Seismic studies of the Brasília fold belt at the western border of the São Francisco craton, central Brazil, using receiver functions, surface wave dispersion and teleseismic tomography. Tectonophysics, 388(1–4), 173–185. https://doi.org/10.1016/J.TECTO.2004.04.029

Assumpção, M., & Sacek, V. (2013). Intra-plate seismicity and flexural stresses in central Brazil. Geophysical Research Letters, 40(3), 487–491. https://doi.org/10.1002/grl.50142

Assumpção, M., Schimmel, M., Escalante, C., Barbosa, J. R., Rocha, M., & Barros, L. V. (2004). Intraplate seismicity in SE Brazil: Stress concentration in lithospheric thin spots. Geophysical Journal International, 159(1), 390–399. https://doi.org/10.1111/j.1365-246X.2004.02357.x

Bangerth, W., Dannberg, J., Gassmöller, R., & Heister, T. (2019). ASPECT v2.1.0 [Computer software]. Zenodo. https://doi.org/10.5281/zenodo.2653531

Barros, L. V., Assumpção, M., Quintero, R., & Caixeta, D. (2009). The intraplate Porto dos Gaúchos seismic zone in the Amazon craton, Brazil. Tectonophysics, 469(1–4), 37–47. https://doi.org/10.1016/J.TECTO.2009.01.006

Barrows, L., & Langer, C. J. (1981). Gravitational potential as a source of earthquake energy. Tectonophysics, 76(3–4), 237–255. https://doi.org/10.1016/0040-1951(81)90099-8

Becker, T. W., Lowry, A. R., Faccenna, C., Schmandt, B., Borsa, A., & Yu, C. (2015). Western U.S. intermountain seismicity caused by changes in upper mantle flow. Nature, 524(7566), 458–461. https://doi.org/10.1038/nature14867

Bianchi, M. B., Assumpção, M., Rocha, M. P., Carvalho, J. M., Azevedo, P. A., Fontes, S. L., Dias, F. L., Ferreira, J. M., Nascimento, A. F., Ferreira, M. V., & Costa, I. S. L. (2018). The Brazilian Seismographic Network (RSBR): Improving seismic monitoring in Brazil. Seismological Research Letters, 89(2A), 452–457. https://doi.org/10.1785/0220170227

Cammarano, F., Goes, S., Vacher, P., & Giardini, D. (2003). Inferring upper-mantle temperatures from seismic velocities. Physics of the Earth and Planetary Interiors, 138(3–4), 197–222. https://doi.org/10.1016/S0031-9201(03)00156-0

Coblentz, D. D., & Richardson, R. M. (1996). Analysis of the South American intraplate stress field. Journal of Geophysical Research: Solid Earth, 101(B4), 8643–8657. https://doi.org/10.1029/96JB00090

Craig, T. J., Jackson, J. A., Priestley, K., & McKenzie, D. (2011). Earthquake distribution patterns in Africa: Relationship to lithospheric structure and rheology. Geophysical Journal International, 185, 403–434. https://doi.org/10.1111/j.1365-246X.2011.04950.x

Fernandes, P. R., Tommasi, A., & Vauchez, A. (2021). The São Francisco craton root beneath the Neoproterozoic Brasília belt (Brazil): Petrophysical data from kimberlite xenoliths. Tectonophysics, 816, 229011. https://doi.org/10.1016/j.tecto.2021.229011

Feng, M., van der Lee, S., & Assumpção, M. (2007). Upper mantle structure of South America from joint inversion of waveforms and Rayleigh-wave group velocities. Journal of Geophysical Research: Solid Earth, 112, B04312. https://doi.org/10.1029/2006JB004449

Fraters, M., Bangerth, W., Thieulot, C., Glerum, A., & Spakman, W. (2019). Efficient Newton solvers for non-linear Stokes systems in geodynamics. Geophysical Journal International, 218(2), 873–894. https://doi.org/10.1093/gji/ggz183

Frost, D. J. (2008). The upper mantle and transition zone. Elements, 4(3), 171–176. https://doi.org/10.2113/GSELEMENTS.4.3.171

Ghosh, A., Holt, W. E., & Flesch, L. M. (2009). Contribution of gravitational potential energy differences to the global stress field. Geophysical Journal International, 179(2), 787–812. https://doi.org/10.1111/j.1365-246X.2009.04326.x

Gibson, S. A., Thompson, R. N., Leonardos, O. H., Dickin, A. P., & Mitchell, J. G. (1995). The Late Cretaceous impact of the Trindade mantle plume. Journal of Petrology, 36(1), 189–229. https://doi.org/10.1093/petrology/36.1.189

Goes, S., Govers, R., & Vacher, P. (2000). Shallow mantle temperatures under Europe from P- and S-wave tomography. Journal of Geophysical Research: Solid Earth, 105(B5), 11153–11169. https://doi.org/10.1029/1999JB900300

Heister, T., Dannberg, J., Gassmöller, R., & Bangerth, W. (2017). High-accuracy mantle convection simulations II. Geophysical Journal International, 210(2), 833–851. https://doi.org/10.1093/gji/ggx195

Hirth, G., & Kohlstedt, D. (2004). Rheology of the upper mantle and mantle wedge. Geophysical Monograph Series, 138, 83–105. https://doi.org/10.1029/138GM06

Jones, C., Unruh, J., & Sonder, L. (1996). The role of gravitational potential energy in active deformation. Nature, 381, 37–41. https://doi.org/10.1038/381037a0

Laske, G., Masters, G., Ma, Z., & Pasyanos, M. (2013). Update on CRUST1.0—A 1-degree global model of Earth's crust. Geophysical Research Abstracts, 15, EGU2013-2658.

McKenzie, D., Jackson, J., & Priestley, K. (2005). Thermal structure of oceanic and continental lithosphere. Earth and Planetary Science Letters, 233(3–4), 337–349. https://doi.org/10.1016/J.EPSL.2005.02.005

Molchan, G. M. (1990). Strategies in strong earthquake prediction. Physics of the Earth and Planetary Interiors, 61(1–2), 84–98.

Molchan, G. M. (1991). Structure of optimal strategies in earthquake prediction. Tectonophysics, 193(4), 267–276.

Molchan, G. M., & Kagan, Y. Y. (1992). Earthquake prediction and its optimization. Journal of Geophysical Research, 97(B4), 4823–4838.

Mooney, W. D., Ritsema, J., & Hwang, Y. K. (2012). Crustal seismicity and Mcmax in stable continental regions. Earth and Planetary Science Letters, 357–358, 78–83. https://doi.org/10.1016/j.epsl.2012.08.032

NOAA National Centers for Environmental Information. (2022). ETOPO 2022 15 Arc-Second Global Relief Model. https://doi.org/10.25921/fd45-gt74

Pasyanos, M. E., Masters, T. G., Laske, G., & Ma, Z. (2014). LITHO1.0: An updated crust and lithospheric model of the Earth. Journal of Geophysical Research: Solid Earth, 119(3), 2153–2173. https://doi.org/10.1002/2013JB010626

Schulte, S. M., & Mooney, W. D. (2005). An updated global earthquake catalogue for stable continental regions. Geophysical Journal International, 161(3), 707–721. https://doi.org/10.1111/j.1365-246X.2005.02554.x

Schmalholz, S. M., Medvedev, S., Lechmann, S. M., & Podladchikov, Y. (2014). Tectonic overpressure and gravitational potential energy. Geophysical Journal International, 197(2), 680–696. https://doi.org/10.1093/gji/ggu040

Schimmel, M., Assumpção, M., & VanDecar, J. C. (2003). Seismic velocity anomalies beneath SE Brazil. Journal of Geophysical Research: Solid Earth, 108(B4). https://doi.org/10.1029/2001JB000187

Tesauro, M., Kaban, M. K., & Mooney, W. D. (2015). Variations of lithospheric strength and elastic thickness in North America. Geochemistry, Geophysics, Geosystems, 16, 2197–2220. https://doi.org/10.1002/2015GC005937

Tian, D., et al. (2024). PyGMT: A Python interface for the Generic Mapping Tools (v0.11.0). Zenodo. https://doi.org/10.5281/zenodo.10578540

Turcotte, D. L., & Schubert, G. (2014). Geodynamics (3rd ed.). Cambridge University Press.

Van Decar, J. C., James, D. E., & Assumpção, M. (1995). Seismic evidence for a fossil mantle plume beneath South America. Nature, 378(6552), 25–31. https://doi.org/10.1038/378025a0

Wessel, P., et al. (2019). The Generic Mapping Tools version 6. Geochemistry, Geophysics, Geosystems, 20, 5556–5564. https://doi.org/10.1029/2019GC008515

Figure Captions:

Figure 1 (a) Location of the study area with digital elevation model, taken from ETOPO Global Relief Model (NOAA National Centers for Environmental Information [NCEI], 2022). (b) Seismicity map of Central and Southeastern Brazil. Araçuaí fold belt (AB), Braília fold belt (BB), Ribeira belt (RB), Goiás Massif (GM). Thick dashed line is suture zone proposed by Lesquer et al. (1981). Threshold magnitudes were used to create a uniform earthquake catalogue for the study area (Assumpção et al., 2004). The earthquake epicentral distribution shown in the figure is from the Brazilian Seismic catalogue, collected from the Brazilian Seismic Network or RSBR (Rede Sismográfica Brasileira) (Bianchi et al., 2018) which includes both historical and instrumental data.

Figure 2 (a) 3D spherical shell Model domain with range of latitude, longitude and depth. The marked rectangle shows the mesh refinement implemented in the model. (b) Assumed boundary conditions on the model domain. The top boundary is a free surface, Bottom and most of the side boundary walls are free slip. Traction boundary condition implemented on the top part of the western side wall, the rest of the boundary remains open. This is to consider the east–west compression. Note: This traction boundary condition is not assumed in all the models but just for model a-2. The rest of the models have free slip boundary condition on the western side wall.

Figure 3 Crustal thickness distribution in the study are. (a) upper crust thickness distribution. (b) lower crust thickness distribution. Crustal thickness data are taken from CRUST1.0 (Laske et al., 2013). Refer to figure 1(b) for the abbreviations.

Figure 4 (a-d) P-wave velocity anomalies beneath the study area from Schimmel et al. (2018) at depths of (a) 100 km, (b) 200 km, (c) 400 km, and (d) 600 km. The white line indicates the shoreline, and the black covered area indicates the ocean. (e-h) Inverted temperature anomalies at depths of (e) 100km, (f) 200 km, (g) 400 km, and (h) 600 km.

Figure 5 Seismicity map and thermal structure of the study area. (a) Map and temperature profiles for Model 1s. (b) Map and temperature profiles for Model 2. In both panels, red dashed lines denote the locations of transects AA′ (14°S) and BB′ (20°S). The white line in the temperature profiles represents the contour of 1300 K isotherm, marking the lithosphere-asthenosphere boundary (LAB). The red stars represent earthquake epicentres along the transects.

Figure 6 Surface strain rate distribution for (a) Model 1-1, (b) Model 1-2, (c) Model 2-1, and (d) Model 2-2.

Figure 7 Distribution of (a) Uncompensated and (b) Compensated Elevated Gravitational Potential Energy (GPE) in the study area. The abbreviations in the map are described in Figure 1(b).

Figure 8 Distribution of crustal thickness gradient in the continental part of Brazil. The abbreviations are mentioned in Figure 1(b).

Figure 9 Molchan diagrams evaluating the predictive skill of various spatial models. (a) Comparison of skill (S) values for seismicity against strain-rate distributions for all four numerical models. (b) Comparison of skill values for the Model 2-2 strain-rate distribution with uncompensated (GPE) and compensated (GPEc) gravitational potential energy distributions. In both panels, the black dashed line represents no correlation (S=0). The black solid curve denotes the earthquake distribution representing the upper bound.

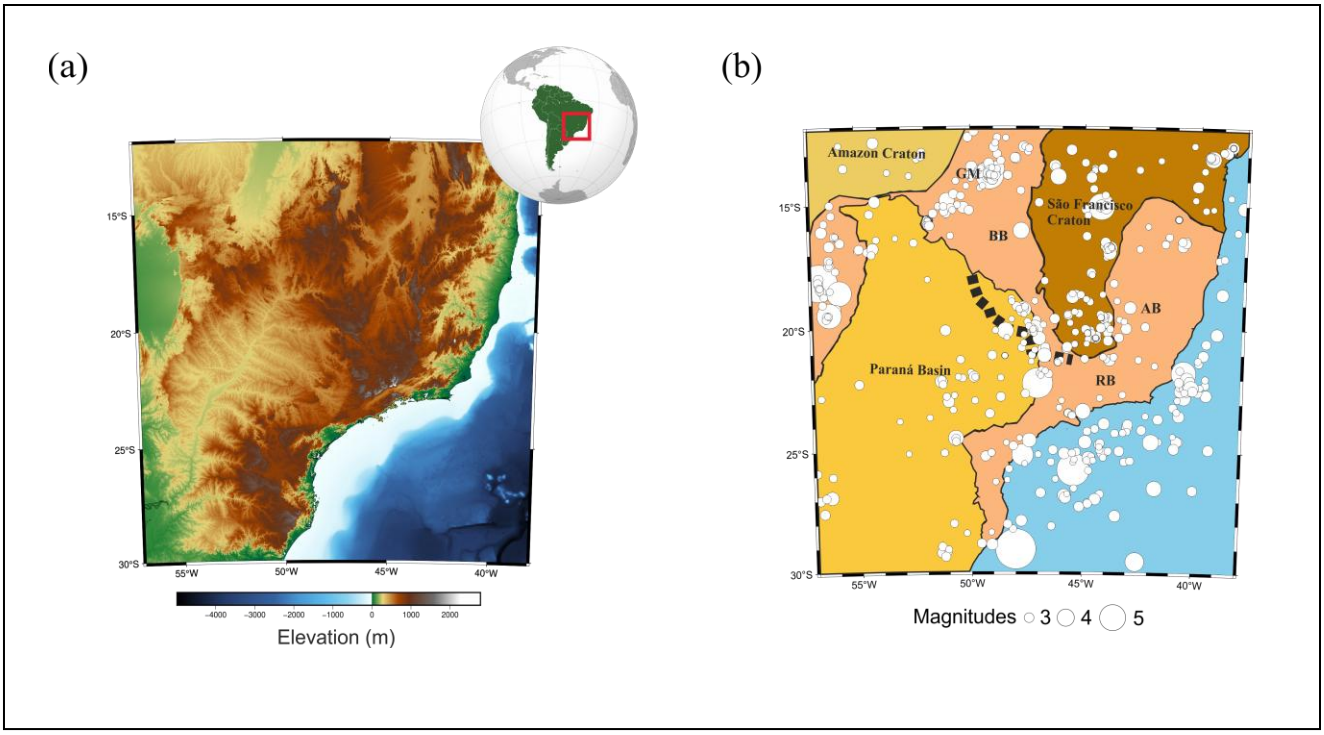
(a)
15°S
20°S
25°S
30°S
55°W
50°W
45°W
40°W
−4000
−3000
−2000
−1000
0
1000
2000
Elevation (m)
(b)
Amazon Craton
GM
São Francisco Craton
BB
AB
Paraná Basin
RB
15°S
20°S
25°S
30°S
55°W
50°W
45°W
40°W
Magnitudes 3 4 5

Figure 1

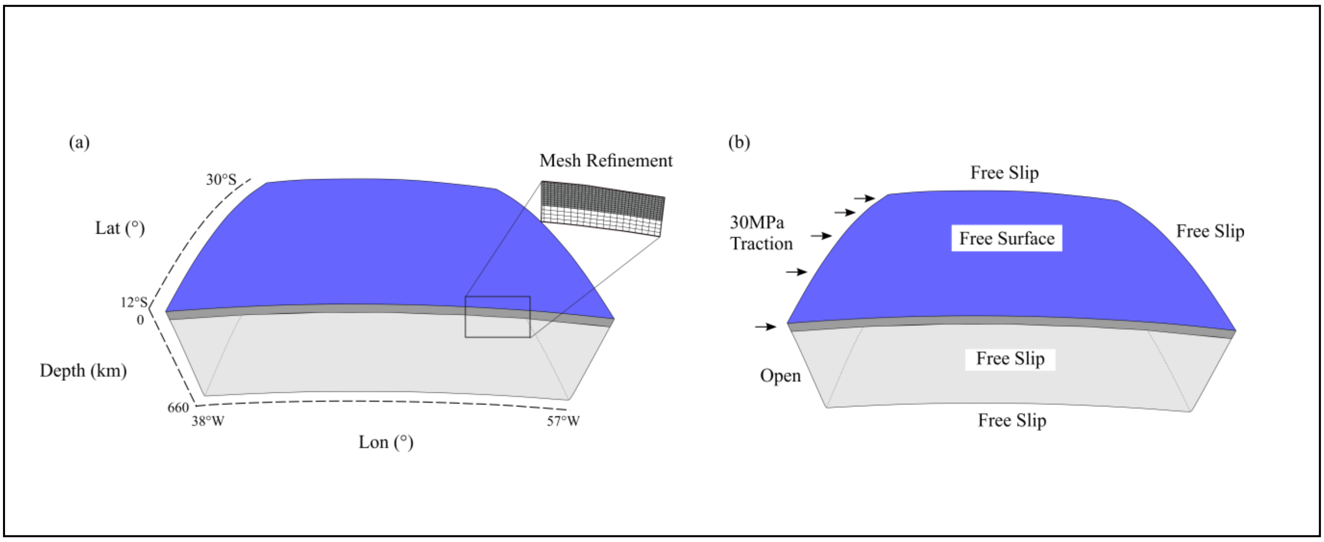
(a)
Mesh Refinement
30°S
Lat (°)
12°S
0
Depth (km)
660
38°W
57°W
Lon (°)
(b)
Free Slip
30MPa
Traction
Free Surface
Free Slip
Free Slip
Open
Free Slip

Figure 2

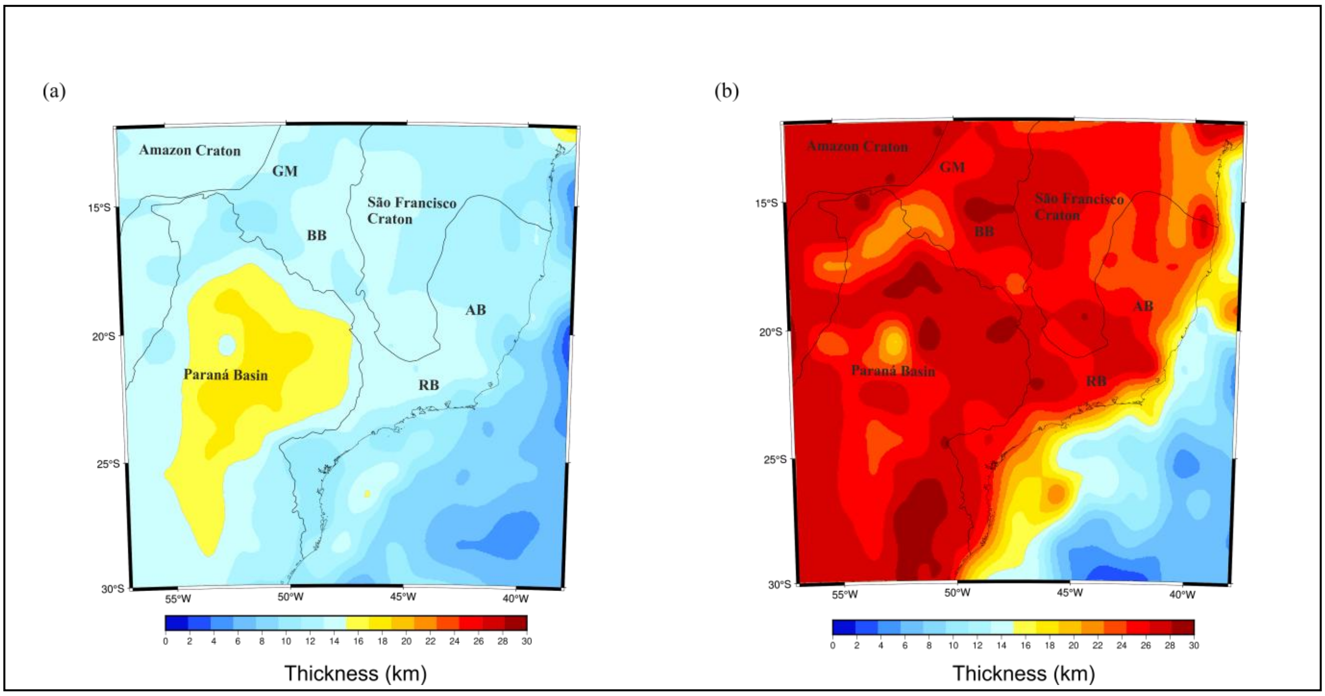
(a)
Amazon Craton
GM
São Francisco
Craton
BB
AB
Paraná Basin
RB
15°S
20°S
25°S
30°S
55°W
50°W
45°W
40°W
0 2 4 6 8 10 12 14 16 18 20 22 24 26 28 30
Thickness (km)
(b)
Amazon Craton
GM
São Francisco
Craton
BB
AB
Paraná Basin
RB
15°S
20°S
25°S
30°S
55°W
50°W
45°W
40°W
0 2 4 6 8 10 12 14 16 18 20 22 24 26 28 30
Thickness (km)

Figure 3

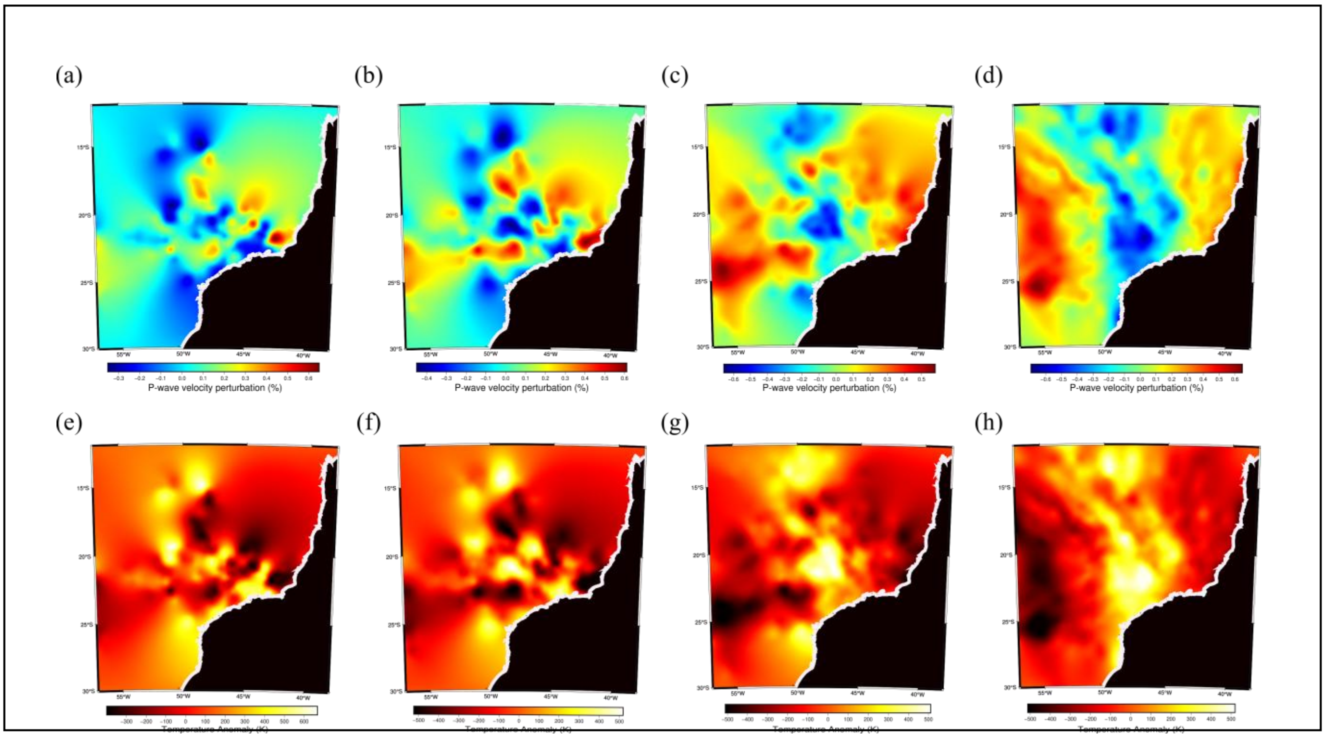
(a)
(b)
(c)
(d)
(e)
(f)
(g)
(h)
P-wave velocity perturbation (%)
P-wave velocity perturbation (%)
P-wave velocity perturbation (%)
P-wave velocity perturbation (%)
15°S
20°S
25°S
30°S
55°W
50°W
45°W
40°W

Figure 4

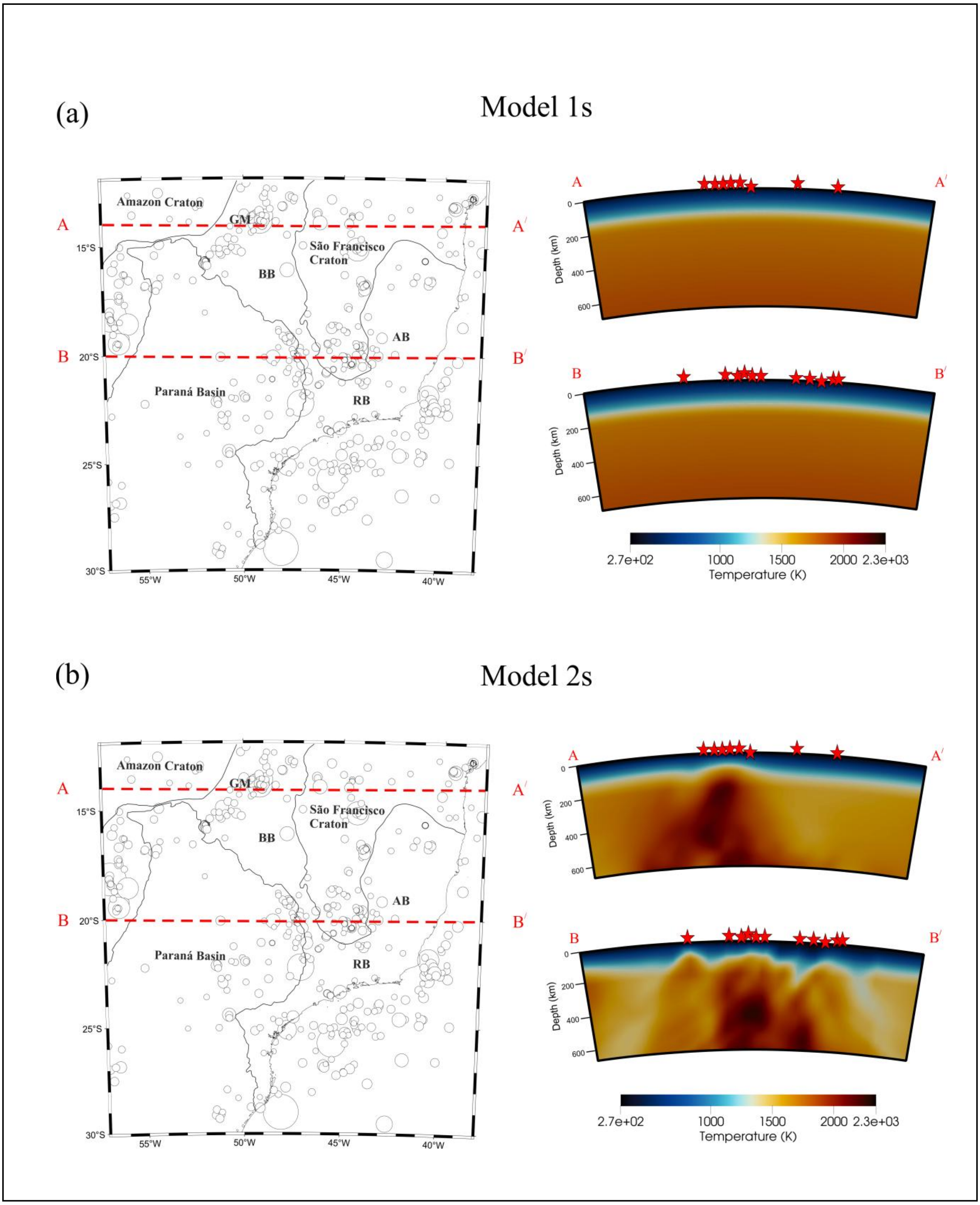
(a)
Model 1s
Amazon Craton
GM
São Francisco Craton
BB
AB
Paraná Basin
RB
A
A′
B
B′
15°S
20°S
25°S
30°S
55°W
50°W
45°W
40°W
Depth (km)
0
200
400
600
2.7e+02
1000
1500
2000
2.3e+03
Temperature (K)
(b)
Model 2s

Figure 5

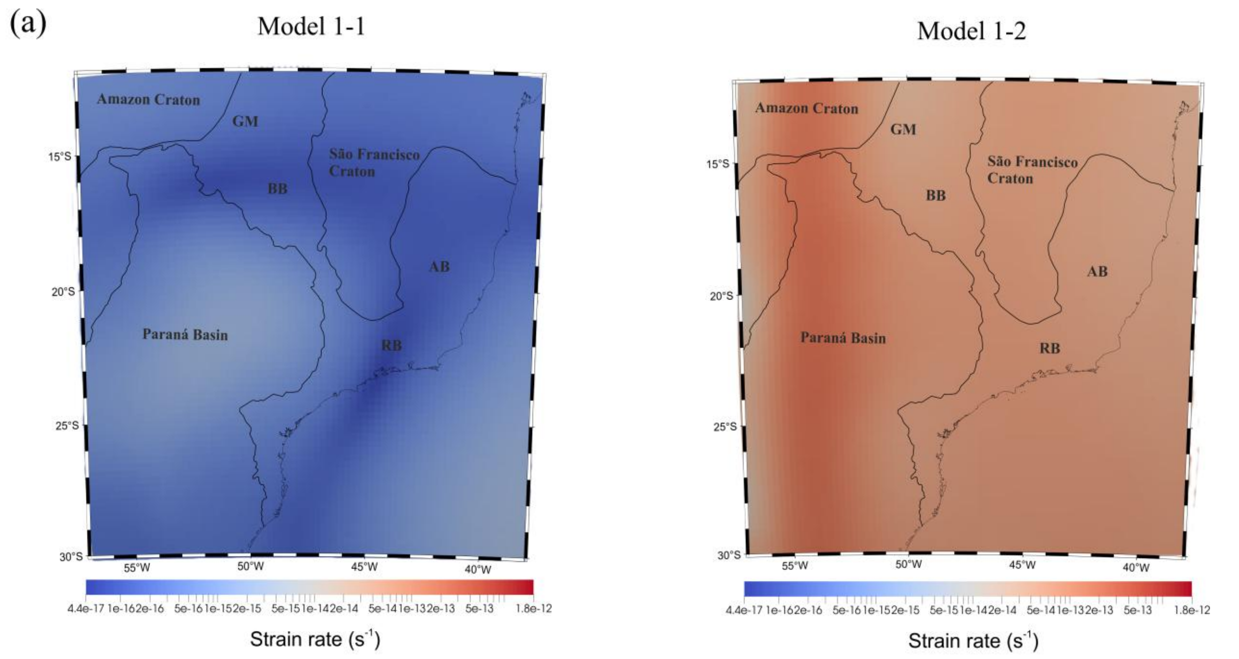
(a)
Model 1-1
Model 1-2
Amazon Craton
GM
São Francisco Craton
BB
AB
Paraná Basin
RB
15°S
20°S
25°S
30°S
55°W
50°W
45°W
40°W
4.4e-17 1e-16 2e-16 5e-16 1e-15 2e-15 5e-15 1e-14 2e-14 5e-14 1e-13 2e-13 5e-13 1.8e-12
Strain rate (s^-1)
(c)
Model 2-1
(d)
Model 2-2

Figure 6

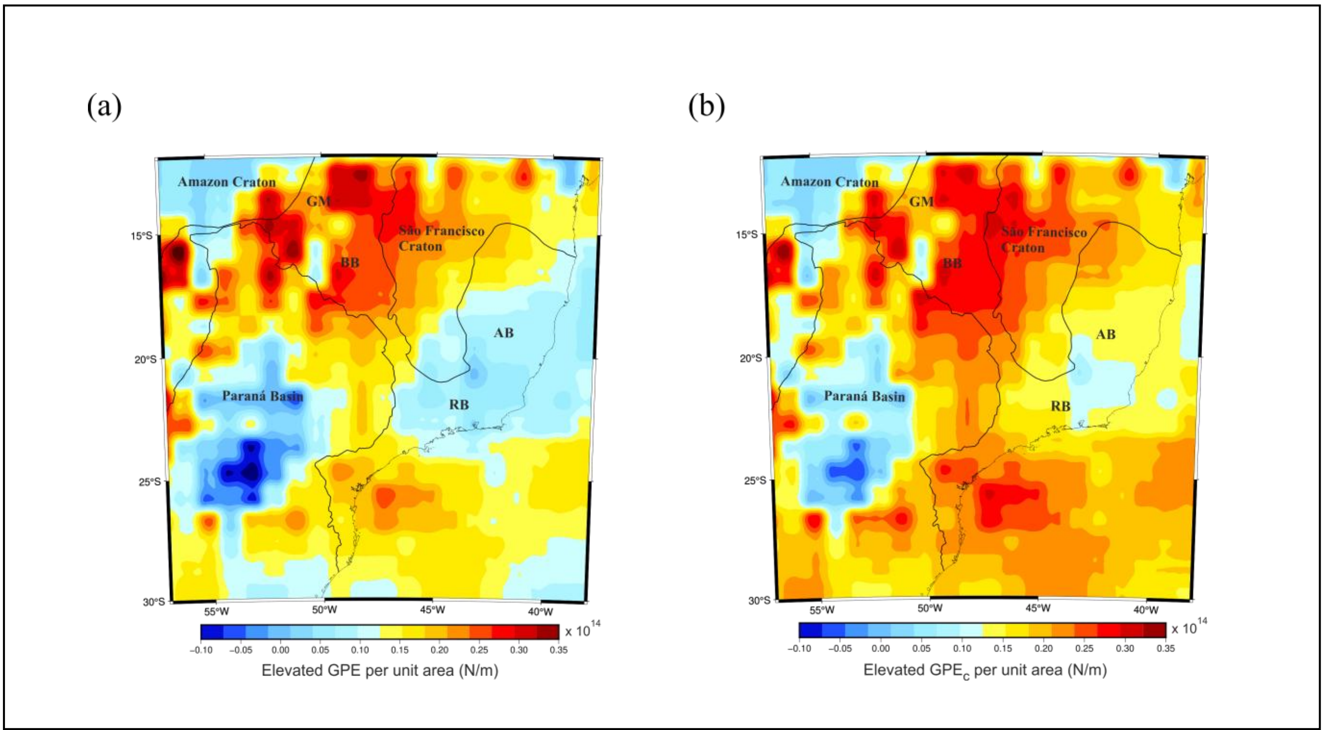
(a)
Amazon Craton
GM
São Francisco
Craton
BB
AB
Paraná Basin
RB
15°S
20°S
25°S
30°S
55°W
50°W
45°W
40°W
x 10^14
Elevated GPE per unit area (N/m)
(b)
Amazon Craton
GM
São Francisco
Craton
BB
AB
Paraná Basin
RB
Elevated GPE_C per unit area (N/m)

Figure 7

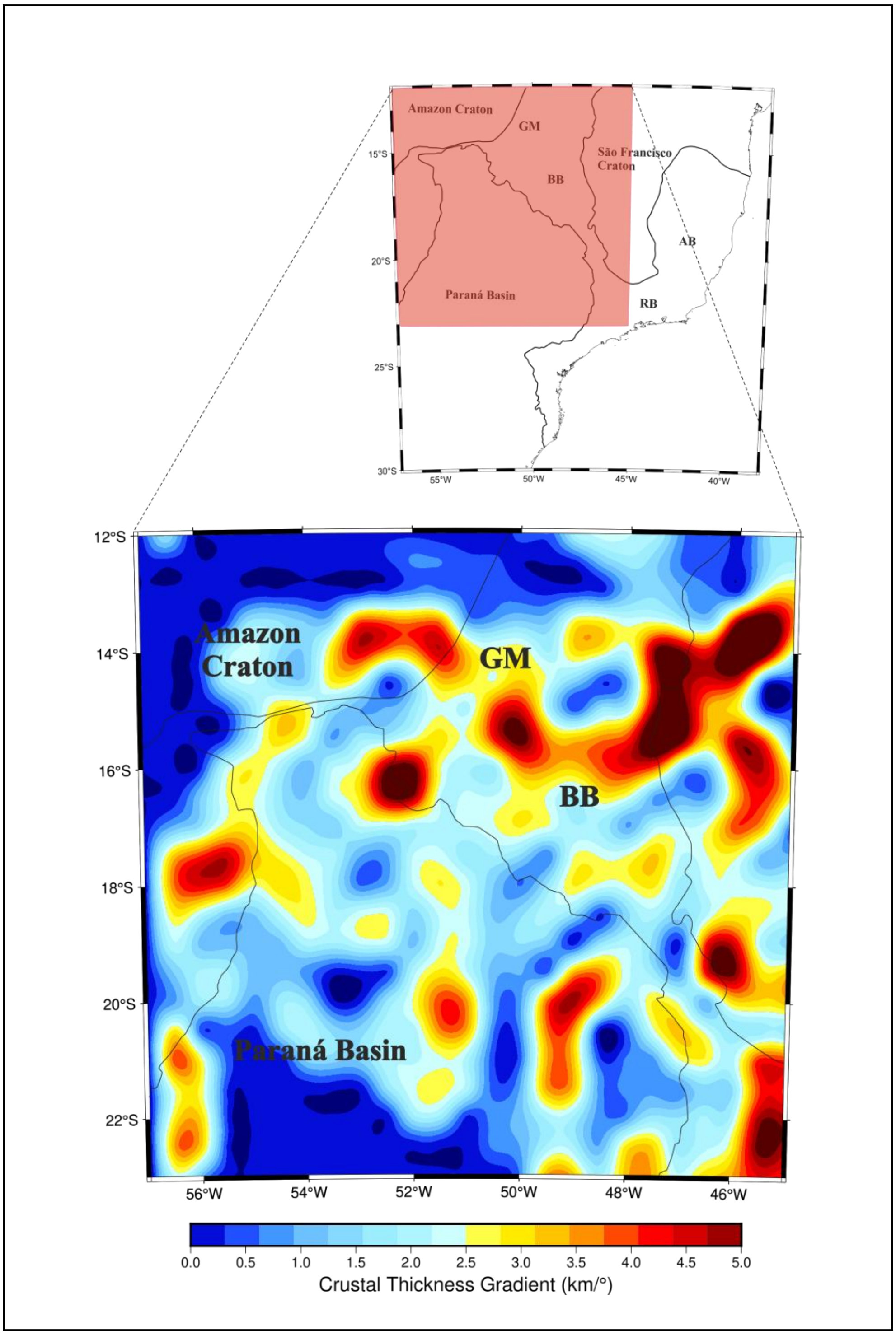
Amazon Craton
GM
São Francisco Craton
BB
AB
RB
Paraná Basin
15°S
20°S
25°S
30°S
55°W
50°W
45°W
40°W
12°S
14°S
16°S
18°S
20°S
22°S
56°W
54°W
52°W
50°W
48°W
46°W
0.0
0.5
1.0
1.5
2.0
2.5
3.0
3.5
4.0
4.5
5.0
Crustal Thickness Gradient (km/°)

Figure 8

(a)

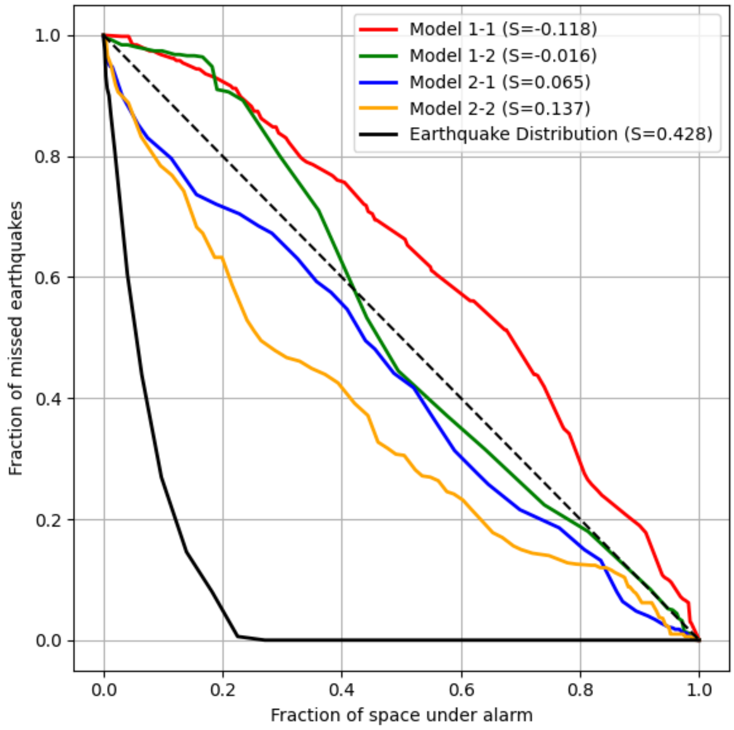
Model 1-1 (S=-0.118)
Model 1-2 (S=-0.016)
Model 2-1 (S=0.065)
Model 2-2 (S=0.137)
Earthquake Distribution (S=0.428)
Fraction of missed earthquakes
Fraction of space under alarm
0.0
0.2
0.4
0.6
0.8
1.0

(b)

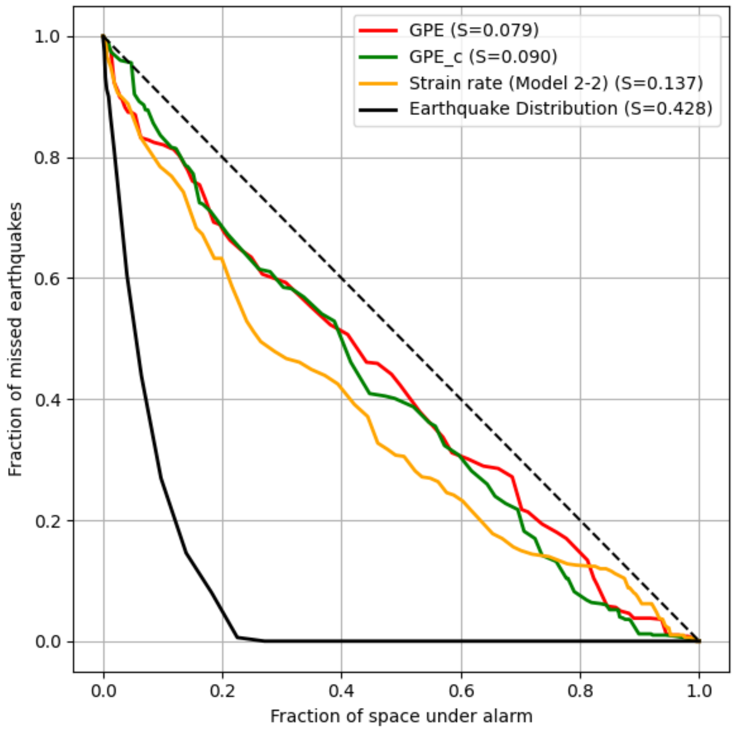
GPE (S=0.079)
GPE_c (S=0.090)
Strain rate (Model 2-2) (S=0.137)
Earthquake Distribution (S=0.428)
Fraction of missed earthquakes
Fraction of space under alarm
0.0
0.2
0.4
0.6
0.8
1.0

Figure 9

Table 1 Material properties for upper crust, lower crust, and mantle.

Property	**Upper Crust**	**Lower Crust**	**Mantle**
Density $(kg\ m^{-3})$	2626	3247	3300
Specific heat $(J\ kg^{-1}K^{-1})$	800	800	1250
Thermal expansion coefficient (K^{-1})	0	0	3×10^{-5}
Thermal conductivity $(W\ m^{-1}K^{-1})$	2.5	2.5	3.3
Rheological parameters for diffusion creep			
Grain size (m)	1×10^{-3}	1×10^{-3}	1×10^{-3}
Pre-exponential factor $(Pa^{-n}m^{mdiff}s^{-1})$	5×10^{-51}	5×10^{-51}	2.37×10^{-15}
Grain size exponent $(mdiff)$	3	3	3
Activation energy $(J\ mol^{-1})$	0	0	3.75×10^{5}
Activation volume (m^3mol^{-1})	0	0	1×10^{-5}
Rheological parameters for dislocation creep			
Pre-exponential factor $(Pa^{-n}s^{-1})$	8.57×10^{-28}	7.13×10^{-28}	6.52×10^{-16}
Stress exponent (n)	4	3	3.5
Activation energy $(J\ mol^{-1})$	2.23×10^{5}	3.45×10^{5}	5.3×10^{5}
Activation volume (m^3mol^{-1})	0	0	1.8×10^{-5}
Angle of internal friction	30	30	30
Cohesion (MPa)	20	20	20

Note: Values for the upper crust are taken from Rutter & Brodie (2004), for lower crust Rybacki & Dresen (2000), for mantle Hirth & Kohlstedf (2003).

Table 2 Nomenclature of different models

Model	Crust thickness	Temperature	B.C.	Chemical composition of the mantle
Model 1-1	CRUST 1.0	Average geotherm	Free kinematic	-
Model 1-2	CRUST 1.0	Average geotherm	30 MPa traction	-
Model 2-1	CRUST 1.0	Inverted from *Schimmel et al.* 2003	Free kinematic	Sp-Peridotite
Model 2-2	CRUST 1.0	Inverted from *Schimmel et al. 2003*	30 MPa traction	Sp-Peridotite

Note: B.C. means boundary condition

Table A.1 *Mineral Physics data used in this study.*

Mineral	Olivine	Orthopyroxene	Clinopyroxene	Garnet	Wadsleyite	Ringwoodite	Plagioclase
$\rho\ (kg\ m^{-3})$	3222	3215	3277	3565	3472	3548	2680
$K\ (GPa)$	129	109	105	171	171	185	84
$G\ (GPa)$	81	75	67	92	112	120.4	40
K'	4.2	7.0	6.2	4.4	4.5	4.1	4
G'	1.4	1.6	1.7	1.4	1.5	1.3	1.1
$\frac{\partial K}{\partial T}\ (GPa\ K^{-1})$	-0.017	-0.016	-0.013	-0.019	-0.014	-0.013	-0.005
$\frac{\partial G}{\partial T}\ (GPa\ K^{-1})$	-0.014	-0.013	-0.010	-0.010	-0.014	-0.010	-0.0068
$a_0\ (10^{-4})$	0.20	0.387	0.3206	0.099	0.232	0.1225	0.234
$a_1\ (10^{-7})$	0.139	0.044	0.0811	0.116	0.0904	0.1104	0.12105
$a_2\ (10^{-2})$	0.1627	0.03435	0.1347	0.604	-0.3966	0.2496	0.5206
$c_{p_0}\ (10^{2})$	1.658	1.855	2.433	1.267	1.7287	1.585	2.909
$c_{p_1}\ (10^{-2})$	0.2332	0.233	0.188	0.2332	1.1294	1.2205	2.76
$c_{p_2}\ (10^{7})$	-0.3971	-0.6326	-0.135	-0.6326	-0.1077	-1.2297	-3.408

Note: ρ: density, K: bulk modulus, G: shear modulus, K': pressure derivative of bulk modulus, G': pressure derivative of shear modulus, $\frac{\partial K}{\partial T}$: temperature derivative of bulk modulus, ∂G: temperature derivative of shear modulus, a_0, a_1, a_2 are constants of thermal expansivity, $\alpha = a_0 + a_1 T + a_2 T^{-1}$, c_{p_0}, c_{p_1}, c_{p_2} are coefficients of heat capacity, $c_p = c_{p_0} + c_{p_1} T + c_{p_2} T^{-1}$. Values of the elastic moduli and their derivatives are from *Cammarano et al.* (*2003*) and thermal expansion coefficients and heat capacity coefficients are from *Saxena and Shen* (*1992*).